Modelling and
Simulation in Materials
Science and
Engineering

PAPER • **OPEN ACCESS**

Virtual design of multilayered SOFC microstructures based on particle packing and spherical harmonics

To cite this article: Lukas Schöller *et al* 2026 *Modelling Simul. Mater. Sci. Eng.* **34** 045013

Modelling and Simulation in Materials Science and Engineering

OPEN ACCESS

RECEIVED
26 January 2026

REVISED
30 April 2026

ACCEPTED FOR PUBLICATION
21 May 2026

PUBLISHED
15 June 2026

PAPER

Virtual design of multilayered SOFC microstructures based on particle packing and spherical harmonics

Lukas Schöller[1,2,*], **Luzie Wehner**[3], **Daniel Schneider**[1,2], **Ruth Schwaiger**[3] and **Britta Nestler**[1,2,4]

[1] Institute of Digital Materials Science (IDM), Karlsruhe University of Applied Sciences, Moltkestraße 30, 76133 Karlsruhe, Germany
[2] Institute for Applied Materials—Microstructure Modelling and Simulation (IAM-MMS), Karlsruhe Institute of Technology (KIT), Kaiserstraße 12, 76131 Karlsruhe, Germany
[3] Institute of Energy Materials and Devices (IMD), Structure and Function of Materials (IMD-1), Forschungszentrum Jülich GmbH, Wilhelm-Johnen-Straße, 52428 Jülich, Germany
[4] Institute of Nanotechnology—Microstructure Simulations (INT-MSS), Karlsruhe Institute of Technology (KIT), Hermann-von-Helmholtz-Platz 1, 76344 Eggenstein-Leopoldshafen, Germany
[*] Author to whom any correspondence should be addressed.

E-mail: lukas.schoeller@kit.edu

Keywords: solid oxide fuel cell, virtual microstructure generation, spherical harmonics, multiphase-field method, microstructure reconstruction, multi-objective optimization

Abstract

Realistic three-dimensional reconstructions of solid oxide fuel cell (SOFC) microstructures are essential for understanding structure-property relationships and optimizing performance. This work presents a physics-informed, stochastic microstructure generator that extends existing particle-packing and spherical harmonics-based methods designed for lithium-ion battery electrodes to the more complex, multilayered structures of SOFCs. The approach integrates a discrete element method for realistic sphere packing, an enhanced neighbor graph for inter-particle connectivity, and a spherical harmonics-based shape generation constrained by contact points. The resulting structures are represented using a multiphase-field method and calibrated through a multi-objective Bayesian optimization framework against morphological metrics derived from focused ion beam–scanning electron microscopy tomography, including volume fraction, tortuosity, specific surface area, and equivalent radius distributions. The method accurately reproduces both porous and dense SOFC layers, as well as complete multilayer structures, achieving low deviations from experimental data and strong visual agreement. This generator enables the efficient and systematic generation of virtual SOFC microstructures with controllable morphological properties and multiphase-field representations suitable for subsequent morphology-resolved simulations. It therefore provides a versatile framework for microstructure design and for preparing calibrated virtual structures for further electrochemical, electro-chemo-mechanical, or degradation studies.

1. Introduction

Solid oxide fuel cells (SOFCs) are a promising technology for efficient energy conversion due to their high operating temperatures, fuel flexibility, and long-term stability [24, 66]. Related advances in solid oxide electrolysis cells, proton-conducting solid oxide cells, and direct-ammonia SOFC concepts further highlight the broad technological relevance of solid oxide electrochemical systems and the need for tailored microstructures and materials design [19, 38, 48]. The durability of SOFC components remains important for practical deployment [39]. This includes challenges related to mechanically robust electrode architectures, durable interconnect materials, and stable electrode and cathode surface chemistry under operation [27, 34, 39]. One of the most critical factors influencing SOFC performance is the microstructure of the individual layers, particularly in the electrode and electrolyte regions. These microstructures govern essential properties such as transport efficiency, mechanical integrity, and electrochemical activity through morphological features like volume fraction, tortuosity, specific surface area (SSA), and triple phase boundary (TPB) density [7, 27, 34, 35]. Despite advancements in experimental

characterization techniques, the analysis of SOFC microstructures remains limited by current imaging techniques. Focused ion beam-scanning electron microscopy (FIB-SEM) tomography, while powerful, is constrained by high costs, long acquisition times, and the relatively small volumes that can be analyzed [6, 12, 62]. Additionally, inherent variability in experimental samples due to fabrication inconsistencies can obscure systematic investigations of morphology-property relationships. To address these challenges, the generation of virtual microstructures has emerged as a powerful complementary approach. Such virtual structures enable the controlled variation of microstructural parameters and are particularly well-suited for parametric studies, numerical simulations, and digital material design.

More recently, machine learning techniques such as artificial neural networks [63], generative diffusion artificial intelligence [42] and generative adversarial networks [16, 23] have shown promise in synthesizing microstructures from 3D training data. These techniques have also been combined with convolutional neural networks [41], for example. While these methods can capture complex features and offer high-speed generation, they often require extensive datasets and lack physical interpretability. Compared with purely data-driven approaches, the present framework provides directly interpretable input parameters, without requiring large 3D training data volumes, and allows layer-specific morphological characteristics to be prescribed in a transparent manner. This is particularly advantageous for multilayer SOFC structures, where porous and dense layers with different functions must be generated in a controlled and physically consistent way.

Stochastic reconstruction methods, which match statistical descriptors such as porosity or correlation functions, allow efficient sampling of microstructures but often fail to accurately represent TPBs and particle connectivity [64, 65]. Feinauer *et al* [14] introduced a stochastic modeling approach that uses Gaussian random fields defined on the sphere to represent particle shapes. This method, designed for battery electrode modeling, enabled controlled sampling of irregular particle geometries via spherical harmonics and facilitated statistical reproduction of shape characteristics observed in experimental datasets. Extending this concept, Westhoff *et al* [60] developed a structure generation approach for lithium-ion battery electrodes, combining particle packing with shape modeling and neighborhood graph construction. Their method used a force-biased packing algorithm along with a minimum spanning tree (MST) based contact network to define inter-particle connectivity. The resulting microstructures could reproduce particle clustering and distributions observed in tomographic data. Although it was originally developed for battery materials, the general framework can be adapted for use with other types of heterogeneous porous media.

To the authors' knowledge, no method has so far been published that enables the systematic generation of virtual microstructures comprising multiple distinct layers with individually controllable morphological properties. Most existing approaches are restricted to single-layer or morphologically homogeneous domains, whereas real SOFCs consist of stacked porous and dense layers with fundamentally different functions and microstructures. This work addresses this gap by introducing a physics-informed structure generator explicitly designed for multilayer SOFC architectures. The aim is not to compete with data-driven approaches in terms of generation speed after training, but to provide a transparent and physically grounded framework for the targeted design and systematic investigation of layer-specific microstructures.

In this work, we extend and adapt the methodology of Westhoff *et al* [60] to develop a flexible virtual structure generator specifically designed for multilayered SOFC microstructures. The generator combines a discrete element method (DEM) for realistic particle packing, a neighbor-graph algorithm for inter-particle connectivity, and spherical harmonics for shape generation. The generated microstructures are converted into smooth, continuum-based representations using a multiphase-field method (MPFM), which facilitates analysis and simulation. To ensure close agreement with real structures, the generator is calibrated using a multi-objective Bayesian optimization (BO) framework, targeting experimentally derived metrics such as volume fraction, tortuosity, SSA, and particle size distribution.

The structure of the paper is as follows: section 2 details the methodology, including structure generation, experimental reconstruction, MPFM representation, and optimization. Section 3 presents validation results for both single-layer and multilayer structures. Section 4 discusses the implications of our findings and concludes the work.

2. Methods

This section details the methodology employed in this study, which includes the generation of artificial SOFC microstructures, reconstruction of experimental data, volume element representation using the

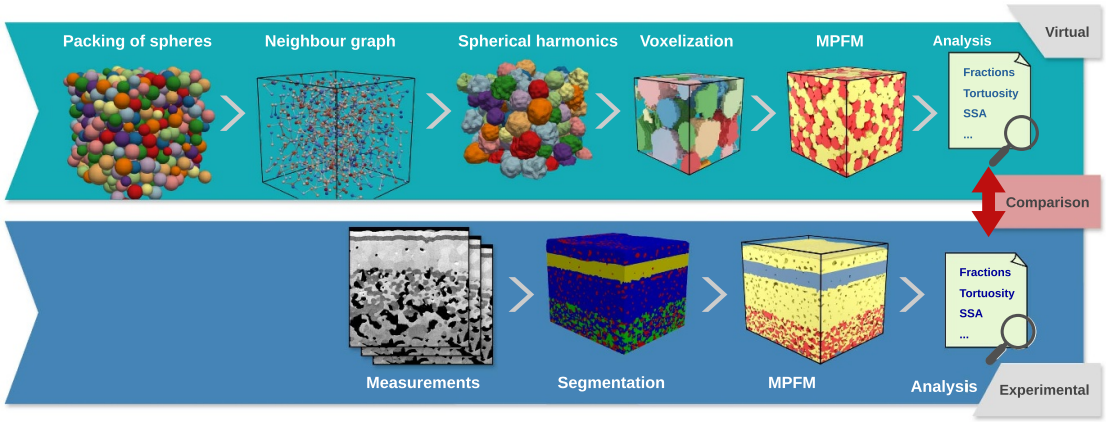

Figure 1. The microstructure generation workflow used in this study is outlined as follows. The generation of virtual microstructures is achieved through the packing of spheres and the use of spherical harmonics, yielding a representation of a volume in the context of the multiphase field method. In contrast, experimental data is used in conjunction with segmentation techniques to reconstruct a multiphase field representation. A comparison is made between the virtual and experimental data using a selection of morphological metrics.

multiphase field method, analysis of morphological metrics, and optimization of generator parameters by a BO. The full workflow is illustrated in figure 1.

2.1. Structure generator

The virtual structure generator used in this work is based on the methods of Feinauer *et al* [14] and Westhoff *et al* [60], originally developed for lithium battery modeling. These methods have been extended to address the specific requirements of multilayer SOFC architectures. The generation process consists of three primary steps:

1. *Packing of spheres*: Based on a discrete element method, hard spheres are packed densely in the domain, respecting particles-size distributions of different materials and different layers of spheres.
2. *Creating a neighbor graph*: Based on the hard spheres packing, contact points are defined. This is done based on a neighbor graph connecting all spheres, minimizing the free length of the connection between the spheres.
3. *Creating particle shapes*: Using spherical harmonics, based on a given angular energy spectra, for each sphere a particle shape is generated. Thereby, the previously defined contact points are considered.

The result of this process is a parametrized microstructure, which is then further processed by a voxelization step and the creation of diffuse interfaces via a MPFM (see section 2.5 for further details).

2.1.1. Packing of spheres

The dense packing of spheres is widely investigated in the literature [2, 17, 36, 37, 53, 57]. The main approaches, without being exhaustive, are either based on the force-biased algorithm or on the discrete element method (DEM). Westhoff *et al* [60] used the force-biased algorithm, which is based on collective rearrangement using a pseudo-force. This method has been shown to achieve dense, non-overlapping packings in both monodisperse [28, 30] and highly polydisperse systems [4]. In contrast, the DEM approach simulates the physical forces acting on particles, including contact models, gravity, and friction [4, 29]. Despite the extensive use of the force-biased algorithm for generating porous microstructures, this work adopts a DEM-based approach. The DEM was first introduced by Cundall and Strack [9] and has become an established method for simulating particle packing, as well as particle flow and particle-fluid interactions. The advantage of DEM lies in its basis in Newtonian mechanics, which simplifies the incorporation of multiple layers within the structure of SOFC microstructures. A comprehensive overview of DEM applications is provided in Zhu *et al* [67, 68]. State-of-the-art software packages such as LAMMPS [56] offer highly efficient and parallelized implementations for large-scale particle packing simulations. In this work, particles are modeled as granular, spherical entities with defined mass, radius, and material type. Their dynamics are described by position, velocity, and force. The pairwise

force between two spherical particles i and j is defined by

$$\boldsymbol{F}^{ij} = \begin{cases} K\delta^{ij}\boldsymbol{n}^{ij}, & \delta^{ij} < 0 \\ 0, & \delta^{ij} \geqslant 0, \end{cases} \qquad \text{with } \delta^{ij} = \left|\boldsymbol{d}^i - \boldsymbol{d}^j\right| - \left(r^i + r^j\right), \tag{1}$$

where $\boldsymbol{d}^i$ is the position vector and r^i the radius of the ith particle, and $\boldsymbol{n}^{ij}$ is the unit vector pointing from particle i to particle j. This models a Hookean spring with a repulsive force between overlapping particles, proportional to the overlap distance δ^{ij}, with a stiffness constant K [52]. Additionally, a viscous damping force

$$\boldsymbol{F}^i = -\gamma \boldsymbol{v}^i, \tag{2}$$

is applied, where $\boldsymbol{v}^i$ is the velocity of particle i and γ is a damping coefficient. This force dissipates energy from the system and leads to energy minimization. Physically, it can be interpreted as mimicking the effect of a viscous medium, such as a particle suspension in processes like screen printing.

At the beginning of the packing simulation, particles are placed randomly in their assigned SOFC layer. To enforce layer separation, particles that attempt to cross a boundary are reflected: their updated position is mirrored and the velocity direction is flipped [5]. Unlike traditional DEM simulations for granular media, gravitational forces are not applied here, as it introduces anisotropy that is undesirable in dense packing scenarios. The system is assumed to be governed mainly by the pairwise interaction force in equation (1) and the damping force in equation (2). The domain is treated as periodic. However, in the stacking direction, where multiple SOFC layers are placed, the domain is non-periodic. The Euler–Lagrange equations are integrated using a velocity Verlet algorithm [58]. To prevent excessive initial overlap, particles are initially placed in a domain larger than the final target size. During the packing procedure, the simulation-box dimensions are gradually reduced toward the target domain size while keeping the particle radii fixed. This compression promotes stable energy minimization without abrupt particle interactions. Once the target density is reached, the system is allowed to equilibrate, with the damping force in equation (2) removing the remaining kinetic energy. The result is a packed configuration that reflects the target volume fractions and particle distributions for each material and layer.

Although completely non-overlapping packing is ideal, it is generally unattainable. However, the minor overlaps that remain are considered negligible, especially in context of the additional particle-shape variation introduced during shape generation using spherical harmonics, and the discretization artifacts arising during voxelization.

2.1.2. Creating a neighbor graph

In the next step, a neighbor graph is created to define contact points between particles. These contacts are essential constraints used in the subsequent particle shape generation stage. The graph is constructed using a MST approach [33], which ensures that all particles are connected through a set of edges with the minimum total weight and no cycles. In our implementation, the neighbor-graph construction operates on the converged DEM packing. The weight of each edge is determined by the free distance between particles δ^{ij}, as introduced in equation (1), i.e. by the gap between particle surfaces beyond their radii.

This distance represents how far apart particles are beyond their radii. The MST ensures that every particle is at least minimally connected within the domain using the shortest possible edge lengths. This procedure follows the same approach described by Westhoff *et al* [60]. However, a pure MST is not sufficient for accurately representing realistic sintering behavior in SOFC structures, where many particles may be in close contact. The MST alone produces a graph with no cycles, which is often too sparse for representing particle neighborhoods in dense systems. Therefore, we introduce several modifications to extend the graph. First, if a particle has other neighboring particles with free distances shorter than the edge in the MST, additional edges are added. Second, up to a defined maximum number of neighbors, further edges are added between particles whose free distances are similar to those already present in the MST. Similarity is determined by both an absolute and a relative threshold compared to existing edge lengths. This ensures that all particles in close proximity are connected, even if they were not part of the original tree.

This extended graph provides a more realistic representation of particle neighborhoods. From the graph contact points are computed for each pair of connected particles. These points are defined as the weighted mean between the centers of the two particles, with the weights based on their respective radii. This weighting accounts for asymmetry in particle sizes and better reflects where physical contact might occur. The final graph, enriched with additional edges beyond the MST, ensures robust connectivity and provides a sufficient number of contact points for enforcing geometrical constraints during particle shape generation. These contact points directly influence the shaping of the particles using spherical

harmonics and ensure that generated particles properly intersect and reflect the connectivity observed in realistic SOFC microstructures.

The neighbor-graph construction defines a geometric connectivity prior at the particle level. It introduces topological connections and corresponding contact-point constraints for the subsequent particle-shape generation, but it does not by itself quantify electrochemically active connectivity. Quantities such as electrochemically active surface area or active TPB density would additionally require criteria and connectivity analysis at the voxel or phase-field level, which are beyond the present calibration targets.

2.1.3. Creating particle shapes

In the final step of the microstructure generation process, individual particle shapes are created using spherical harmonics. This technique allows us to describe realistic, irregular particle surfaces while preserving overall shape statistics and enforcing geometric constraints such as the contact points identified in the previous section. The use of spherical harmonics to generate particles is well-established [14, 15, 60]. In this work, the radius of each particle as a function of co-latitude θ and longitude ϕ is described as

$$r(\theta,\phi) = \bar{r}\,(1 + f(\theta,\phi))\,, \tag{3}$$

with the mean radius $\bar{r}$ of the particle. The function $f(\theta,\phi)$ describes the local fluctuations of the radius in terms of a series expansion of real spherical harmonic functions and is given by

$$f(\theta,\phi) = \sum_{l=0}^{\infty} \sum_{m=-l}^{l} c_l^m Y_l^m(\theta,\phi)\,, \tag{4}$$

with the coefficients c_l^m, and $Y_l^m(\theta,\phi)$ are the real-valued spherical harmonic functions of degree l and mode m. Following the convention without the Condon-Shortley phase [21] they are defined as

$$Y_l^m(\theta,\phi) = \begin{cases} P_l^m(\cos\theta)\cos m\phi & m \geqslant 0 \\ P_l^{|m|}(\cos\theta)\sin|m|\phi & m < 0 \end{cases}. \tag{5}$$

In this work $P_l^m(\cos\theta)$ are the 4π-normalized associated Legendre functions [61]. The angular power spectrum $S(l)$ quantifies the contribution of each degree to the overall shape and is defined as

$$S(l) = \sum_{m=-l}^{l} (c_l^m)^2\,. \tag{6}$$

The total power is given by

$$P = \frac{1}{4\pi} \int_{\Omega} f^2(\theta,\phi)\,\mathrm{d}\Omega = \sum_{l=0}^{\infty} S(l)\,. \tag{7}$$

To define the power spectrum, we use a log-normal distribution characterized by a mean and standard deviation of the resulting distribution. This choice controls the nature of radius fluctuations: Low degrees l lead to elongated or ellipsoidal particles, while higher degrees produce more complex, 'bumpy' surfaces. In this study, the log-normal distribution mean is centered at $l = 4$ with a standard deviation of 6, and the total amplitude of the spectrum is scaled by a factor. This provides control over both the complexity and overall roughness of the particles.

The coefficients c_l^m are sampled from a normal distribution and scaled according to the desired angular power spectrum. A maximum degree of $l_{\max} = 15$ is used to truncate the series for computational efficiency. This level of truncation strikes a balance between particle realism and generation time.

The spherical-harmonics representation therefore introduces controlled particle-shape irregularity up to the chosen truncation level. In the subsequent workflow, the voxelized particles are converted into a diffuse multiphase-field representation, which replaces sharp voxel interfaces by smooth diffuse interfaces. As a result, very small-scale or sub-voxel roughness is smoothed, whereas the larger-scale particle-shape irregularity is retained. This effect should not be confused with the morphological dilation step used later for dense layers, which is a separate post-processing operation introduced only to increase the phase volume fraction where required.

The amplitude reported in tables 1, 2, 4 and 5 denotes the scaling factor applied to the angular power spectrum $S(l)$, and therefore controls the overall magnitude of the spherical-harmonic radius fluctuations through the total power defined in equations (6) and (7). Finally, the previously defined contact

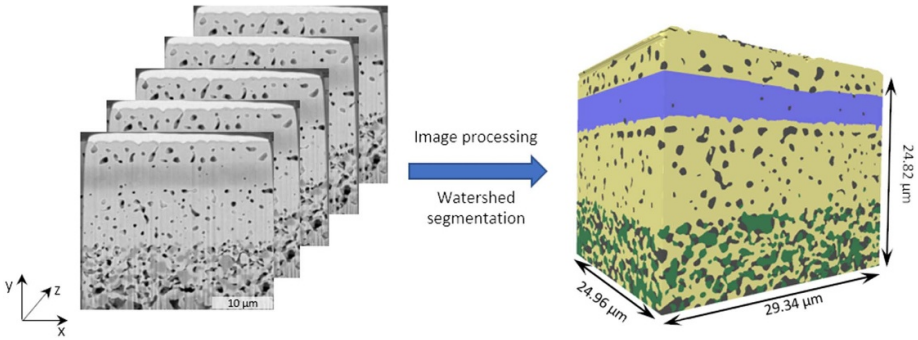

Figure 2. Reconstruction for SOFC microstructures. A stack of images obtained by FIB and SEM tomography is processed and segmented using a watershed algorithm.

points from the neighbor graph are treated as constraints. For the ith constraint, $f(\theta^i, \phi^i) = f^i$ should be fulfilled according to the corresponding contact points. This yields a set of constraints

$$\sum_{l=0}^{\infty} \sum_{m=-l}^{l} c_l^m Y_l^m(\theta^i, \phi^i) = f^i. \tag{8}$$

For multiple contact points, this constraint system can be expressed in matrix form as

$$\boldsymbol{Yc} = \boldsymbol{f}, \tag{9}$$

where $\boldsymbol{Y}$ is the matrix of evaluated spherical harmonics at the contact points, $\boldsymbol{c}$ is the vector of coefficients, and $\boldsymbol{f}$ is the vector of constraint values. To solve this underdetermined system, a singular value decomposition is used, which allows for consistent sampling of random coefficients that still satisfy the contact constraints. This ensures the resulting particle shapes maintain both statistical shape properties and local geometrical constraints. For further implementation details, the reader is referred to the Feinauer *et al* [14].

2.2. Reconstruction of SOFC microstructures

3D data of real microstructures can be obtained by dual beam FIB/SEM tomography. Altering FIB milling and SEM imaging yields a series of consecutive images of a certain volume of interest (VOI). By stacking these images and expanding every pixel in the stacking direction to make it a voxel (volumetric pixel), a 3D reconstructed volume is obtained. From the segmented data several microstructural parameters, such as volume fractions, tortuosity and TPBs, can be calculated. Segmentation, the assignment of every voxel to a material phase based on its gray scale value, of the data set leads to a material distribution in the VOI. Different algorithms, such as local threshold, region growth or watershed, have been developed for the segmentation process [10, 59]. For the watershed segmentation the images are interpreted as topographical reliefs and every pixel's gray scale value corresponds to a height on the image plane. Phase boundaries are stored in an edge map. Starting from local minima the image is flooded until every pixel is assigned to a material phase. In order to reduce errors during the segmentation process, a sufficient image quality, e.g. good material contrast, no gradient in brightness or contrast and low noise, is crucial. Preliminary image processing is important to enhance the image quality by adjusting brightness and contrast, and reducing noise while preserving edges. Minor segmentation errors can be corrected by further image processing. Morphological filters such as erosion and dilation and their combination allow for these corrections, however, they can alter the microstructure significantly if not used with caution. The reconstruction and segmentation workflow is illustrated in figure 2.

Experimental. The cell was manufactured by screen-printing of the Ni-GDC fuel electrode and three electrolyte layers on a Ni-YSZ substrate and co-fired at 1400 °C for 5 h. A detailed description of the cell manufacturing can be found in [46]. For the three-dimensional reconstruction a Helios 5 CXe (Thermo Fischer Scientific, Hillsboro, Or, USA) was used. To protect the cells microstructure while milling, the volume for analysis was covered with a mixture of 99% platinum and 1% carbon. A series of 313 consecutive images resulting in a volume of 18 176 μm^3 was recorded using a backscattering detector. Avizo (Version 2023.1.1, Thermo Fischer Scientific, Hillsboro, Or, USA) was utilized for the reconstruction

process including alignment, filtering and segmentation of the 3D data. The analyzed volume contained the three-layer GDC-YSZ-GDC electrolyte and the Ni-GDC fuel electrode functional layer.

2.3. Multiphase-field representation

The MPFM has become a standard tool for simulating microstructure evolution in materials science, e.g. [31]. It describes particles or grains using smooth scalar fields, called phase fields or order parameters, which vary continuously between one inside a particle and zero outside. Interfaces are captured implicitly through this diffuse transition, avoiding the need for explicit interface tracking or sharp boundaries. This avoids the cumbersome meshing process and loss of accuracy associated with an exclusively voxelization process. Although the present calibration focuses on morphological descriptors, the generated microstructures provide geometrically well-defined input for subsequent SOFC simulations. In particular, the phase volume fractions determine the amount of electronically and ionically conducting material, tortuosity governs effective transport pathways, and the SSA characterizes the extent of reactive interfaces. Together with phase connectivity, these quantities provide the geometric basis for continuum descriptions of ionic/electronic transport, charge-transfer, and reaction kinetics. Owing to their multiphase-field representation, the generated domains can be coupled naturally to electrochemical, electro-chemo-mechanical, or degradation models. In this context, MPFM-based microstructures have also been used to model continuum-based SOFC processes such as nickel coarsening [22], fluid flow [47], or crack propagation [50].

The MPFM used in this study was introduced by Nestler *et al* [40] and Steinbach and Pezzolla [54]. A continuum thermodynamic approach to the phasefield method is described in [45]. In its classical form, the MPFM minimizes the system's curvature. To avoid this, the evolution equations for the phase fields are adapted to prevent curvature minimization. Sun and Beckermann [55] provide a detailed description, and applications can be found in [13, 49]. As realistic microstructures may contain hundreds or thousands of particles, storing a separate order parameter field globally for each particle would lead to prohibitive memory and computational costs. To overcome this, the local reduced order parameter method [25, 32] is used, which defines order parameters only in the local region around each spatial point. This drastically reduces storage requirements and computational costs, while ensuring that particles remain locally distinguishable and fully resolvable.

2.4. Morphological metrics

To quantitatively compare real and artificial SOFC microstructures, several morphological quantities are evaluated for each material phase. These quantities are selected based on their physical relevance to SOFC performance and their sensitivity to microstructural variations. The metrics include volume fraction, tortuosity, SSA and equivalent radius distribution.

TPB density is a commonly used metric for characterizing electrochemical activity in SOFC electrodes. In the present work, TPB density was not selected as an optimization target because it is highly sensitive to local connectivity and segmentation details, and the smallest resolved length scales, which makes a robust TPB-based calibration difficult within the current framework. The present study therefore focuses on morphological descriptors that can be calibrated more robustly at the mesoscale, namely phase fractions, tortuosity, SSA, and, for dense layers, equivalent radius distributions. An explicit TPB-based analysis is left for future work with a stronger electrochemical focus.

Descriptors such as two-point correlation functions could provide complementary information on spatial statistics, but were not included in the present calibration in order to keep the optimization focused on a limited set of robust target quantities.

2.4.1. Volume fraction

The volume fraction v_{f}^{α} of a phase α is calculated as the spatial average of its corresponding phase-field variable ϕ^{α} over the domain

$$v_{\mathrm{f}}^{\alpha} = \frac{1}{V}\int_{V} \phi^{\alpha}\,\mathrm{d}v, \tag{10}$$

where V is the total volume of the domain. Many effective characteristics of the microstructure are dominated by these volume fractions. For example, the linear and harmonic interpolation of the stiffnesses of each material with its volume fraction depict energetic bounds of the effective elastic material behavior [20].

2.4.2. Tortuosity

Tortuosity is a significant quantity for estimating the effective transport properties of a porous microstructure. For example, it can be geometrically defined by comparing the length of a curved path to that of a straight line. In this work, a more physical interpretation of tortuosity is used. Based on a generic diffusion equation, the tortuosity factor can be obtained by solving a Laplace equation, which mimics a steady-state diffusive flow through a material, for example. Then the tortuosity follows by

$$\tau^{\alpha} = \frac{v_{\mathrm{f}}^{\alpha} D}{D_{\mathrm{eff}}}, \tag{11}$$

with the diffusivity coefficient D of the Laplace equation and the calculated effective diffusivity coefficient D_{eff} from the solution. For any material, the condition $\tau^{\alpha} \geqslant 1$ holds, with $\tau^{\alpha} = 1$ for straight paths from one side to the other and with $\tau^{\alpha} > 1$ the microstructure restricts the flow. For a detailed overview of the algorithm used, the reader is referred to Cooper *et al* [8].

2.4.3. SSA

The SSA is defined as the ratio between the surface area and the volume of a material. It is often used when the underlying physical process depends on the surface, such as in adsorption processes or chemical reactions. In the context of the MPFM, it is defined as

$$\mathrm{SSA}^{\alpha} = \frac{A^{\alpha}}{V^{\alpha}}, \qquad \text{with } V^{\alpha} = \int_V \phi^{\alpha}\,\mathrm{d}v, \qquad A^{\alpha} = \int_V |\nabla \phi^{\alpha}|\,\mathrm{d}v, \tag{12}$$

where ϕ^{α} is the order parameter of a material α and its spatial gradient $\nabla\phi^{\alpha}$.

2.4.4. Equivalent radius distribution

In cases where materials exhibit high volume fractions (e.g. dense layers), tortuosity and SSA may become less informative. In such instances, the equivalent radius distribution provides a useful quantity. Assuming particles are approximately circular in 2D slices (e.g. from EBSD data), the equivalent radius r^i of the ith particle can be computed from its area by

$$r^i = \sqrt{\frac{1}{\pi}\int_V \chi^i\,\mathrm{d}a} \tag{13}$$

where χ^i is the indicator function of the particle. Aggregating these values yields a radius distribution, which is approximated by a Gaussian function by fitting its mean μ^{α} and standard deviation σ^{α}, as illustrated in figure 6.

The equivalent radius distribution used for dense layers is derived from 2D EBSD cross-sections and therefore inherits the usual stereological limitation that sectioned particle sizes do not uniquely determine the full 3D grain-size distribution. In the present study, this descriptor is used as a practical surrogate because dense layers contain a dominant phase and conventional porous-microstructure metrics become less informative. The calibration should therefore be interpreted as matching an experimentally accessible 2D proxy rather than reconstructing the full 3D grain topology uniquely.

2.5. Multi-objective BO

The structure generator described in this work depends on several input parameters, such as particle size distributions and angular power spectra, which influence the resulting microstructural properties. However, the relationship between these parameters and the morphological quantities is generally unknown. To address this, we employ multi-objective BO to systematically calibrate the generator so that the output microstructures closely match experimental targets. BO is particularly well-suited for problems where evaluations are computationally expensive and gradients are unavailable. In our case, the objective is to minimize the error between the morphological metrics of generated and experimental structures across multiple objectives. Classical BO methods often rely on Gaussian Processes to model the objective function. However, an alternative method known as the tree-structured Parzen estimator (TPE) offers a robust performance in high-dimensional, conditional search spaces [3]. With the multiple morphological quantities, a multi-objective BO is conducted. To this end, a TPE is used which performs an independent sampling of a single parameter without considering any relationship between parameters. For a more detailed discussion of multi-objective TPE, the reader is referred to Ozaki *et al* [43, 44]. In order to optimize the objective functions, multiple trials are iteratively carried out, each with the following steps within the optimization framework Optuna [1]:

1. *Parameter selection*: The TPE sampler proposes a set of generator input parameters based on the results of previous trials, except for the initial trials, when they are randomly selected from the parameter space.
2. *Particle generation*: Based on the parameters, spheres are packed and contact points are defined via the generator process as described in section 2.1. The created particles are parameterized by spherical harmonics.
3. *Voxelization and volume fraction adjustment*: The particle shapes are voxelized at a high resolution, then downsampled to the desired resolution using interpolation. To approximate the effects of sintering in dense layers, morphological dilation operations are optionally applied to increase volume fraction where needed [18]. This mimics the sintering process of a dense layer where the desired volume fraction is too high for the generator to obtain on its own.
4. *Evolution of diffuse interfaces via a MPFM*: The voxelized structure is converted into a diffuse microstructure using the MPFM detailed in section 2.3. This step ensures smooth interfaces for subsequent analysis despite the use of a uniform grid.
5. *Morphological analysis*: Various morphological metrics are chosen and evaluated based on the properties of the volume element, as discussed in section 2.4.
6. *Objective evaluation*: For each morphological quantity φ, an error is calculated. For a generic metric φ, the error is defined as

$$e_\varphi = \begin{cases} |\varphi - \varphi^\star|, & \text{for volume fraction,} \\ \left|\dfrac{\log_{10}\varphi - \log_{10}\varphi^\star}{\log_{10}\varphi^\star}\right|, & \text{for tortuosity,} \\ \left|\dfrac{\varphi - \varphi^\star}{\varphi^\star}\right|, & \text{otherwise,} \end{cases} \tag{14}$$

7. where $\varphi^\star$ denotes the corresponding target value. The final representative trial is selected by minimizing the Euclidean norm of the resulting objective-error vector. The logarithmic form used for tortuosity treats multiplicative deviations more uniformly across porous and dense layers, whose tortuosity values may differ substantially in scale. No additional weighting factors were introduced in the present study, in order to avoid a subjective prioritization among the target metrics.

Each trial results in a set of objective values. As is standard in multi-objective optimization, no single solution minimizes all objectives simultaneously. Instead, a Pareto front of optimal trade-offs is constructed. To identify a single 'best' set, we select the trial with the minimum Euclidean norm of the objective errors across all metrics. This optimization strategy enables systematic calibration of the structure generator, ensuring that the synthetic microstructures closely replicate key morphological features of real SOFC layers across both single and multilayer configurations.

The proposed optimization framework also allows the structure generator to be used in a forward-design mode. By prescribing target values for selected morphological metrics, such as tortuosity or SSA, these quantities can be directly included as objectives in the BO. The resulting optimization process identifies suitable generator parameters that produce microstructures with the desired properties. Beyond this calibration task, the accumulated trials reveal local parameter–response trends within the explored design space. In particular, they reveal how variations in individual input parameters influence the resulting morphological descriptors, enabling efficient generation of structures with specified characteristics without requiring extensive retraining or experimental input. These trends should not be interpreted as a formal global sensitivity or uncertainty analysis, which would require a dedicated study beyond the scope of the present work.

The computational cost of the workflow is dominated by DEM packing, voxelization and MPFM conversion, and the repeated evaluations required by BO. For this reason, reduced single-layer domains were used during calibration, while the multilayer structure was generated by combining layerwise optimized parameter sets in a divide-and-conquer manner. Qualitatively, the DEM cost scales mainly with the number of particles, whereas memory consumption and MPFM-related cost scale mainly with the number of voxels and the number of locally active order parameters. Increasing domain size, interface resolution, or layer complexity therefore leads to increased wall-clock time and memory demand.

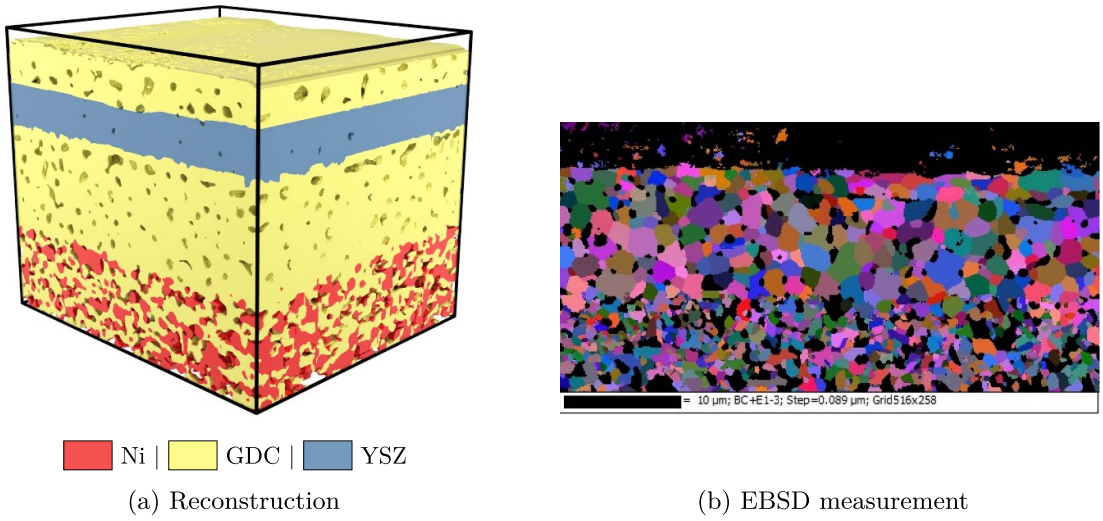

Figure 3. (a) Three-dimensional reconstruction data of the multilayer SOFC, containing the fuel electrode, electrolyte, YSZ, and GDC barrier layers. (b) An electron backscatter diffraction (EBSD) measurement taken across the domain to determine an equivalent radius distribution.

Table 1. Parameters for the generation of the best trial for a fuel electrode layer, cf figure 4(b).

Parameter	Unit	Value Ni	Value GDC
Volume fraction	%	31.91	36.89
Mean particle radius	nm	426.85	353.97
Deviation of particle radius	nm	8.40	65.55
Amplitude of angular power spectrum	W nm^{-1}	$10^{-1.8}$	$10^{-2.5}$
Dilation iterations	—	0	2

3. Results

The approach introduced in section 2 is used to generate an artificial microstructures consisting of a porous fuel electrode, a dense electrolyte layer, and finally a complete multi-layered SOFC structure. During generation, the morphological metrics of the reconstructed cell are used to demonstrate the ability to reproduce realistic microstructures, cf figure 3.

3.1. Fuel electrode layer

To assess the performance of the structure generator in replicating real microstructural features, we first focus on the fuel electrode layer of the SOFC. This layer, composed of GDC (gadolinia-doped ceria) and Ni (nickel), was extracted from the full multilayer reconstruction (cf figures 3(a) and 4(a)). A total of 200 trials were conducted to optimize the generator output, with the objective of matching key morphological metrics: volume fractions, tortuosities, and SSA for both GDC and Ni phases. For this single-layer case study, a reduced simulation domain was chosen to keep the computational cost of the 200-trial optimization manageable while preserving the voxel resolution of the reconstruction. The optimization process varied parameters such as the target volume fraction, the mean and standard deviation of the particle size distributions for each material, and the number of morphological dilation steps applied after voxelization. The amplitude of the angular power spectrum, which influences the surface complexity of the generated particles, was manually selected. This parameter was not included in the optimization loop, as it showed negligible influence on the targeted metrics.

The best result from the optimization is shown in figure 4(b), with quantitative comparison to the reconstructed structure summarized in table 3. The majority of errors are low, with a percentage not exceeding 2.5%. However, the tortuosities exhibit a higher amount of error, i.e 4% to 5%. This is likely due to the existence of individual paths through the volume element that do not homogenize at the same rate as the volume fraction, for example. Figures 4(c) and (d) present the tortuosity fields for both

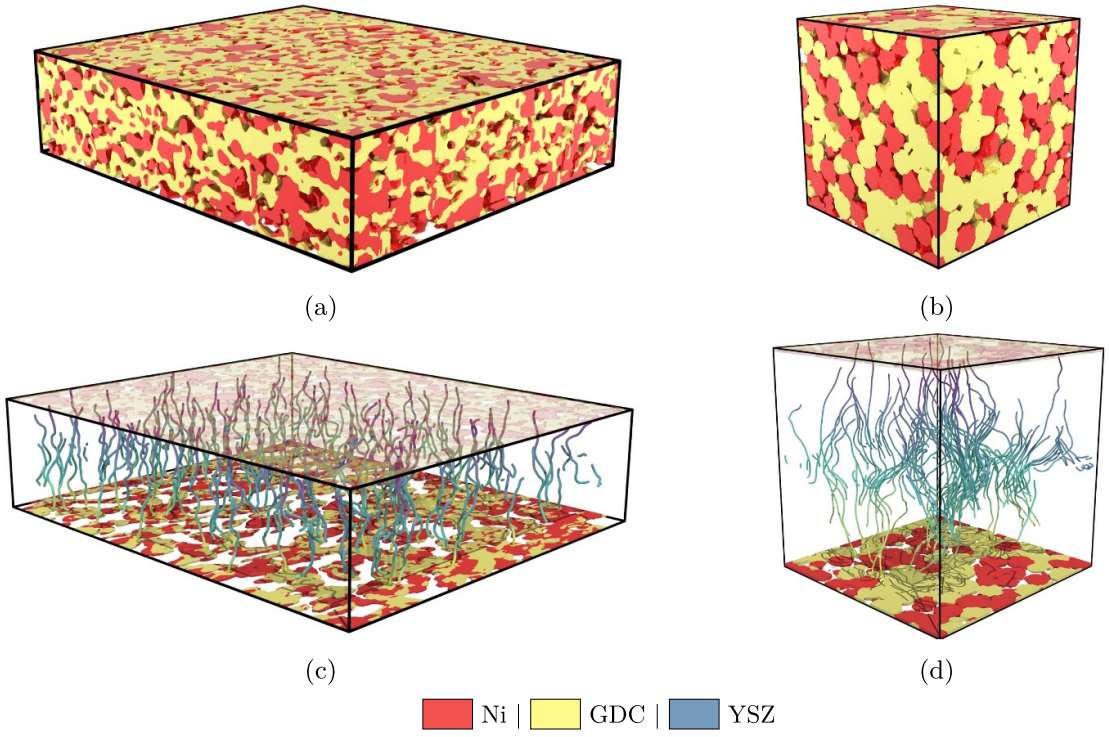

Figure 4. A comparison of the reconstructed fuel electrode layer (a) and the artificially created volume element (b). The streamlines of the potential field obtained by solving the diffusion equation are also displayed for the reconstruction (c) and the artificial volume element (d).

the reconstructed and generated domains. These visualizations display the streamlines of the potential field obtained from solving the diffusion equation, highlighting the similarity in transport pathways between the real and synthetic microstructures. The close visual agreement of the structures as well as in the metrics validates the structure generator's capability to reproduce key features of the porous SOFC fuel electrode layer.

While the previous results focused on matching a specific set of target morphological metrics, generating a different virtual microstructure with alternative target properties would require adjusting the input parameters accordingly. For example, a new optimization run comprising 200 trials could be performed to identify a new set of parameters.

However, a key advantage of the multi-objective BO approach used in this study is that it also builds a database during the optimization process that links the input parameters to the resulting morphological descriptors. This database can also be interpreted as exploratory local parameter screening within the explored parameter space. Figure 5 illustrates these parameter–response trends. In figures 5(a) and (b), a clear relationship between the prescribed input volume fraction and the final volume fraction of Ni and GDC can be observed. In addition, the number of dilation steps causes a noticeable shift in the resulting phase fractions, highlighting its strong influence on this metric. Similarly, in figures 5(c) and (d), the SSA shows a strong inverse correlation with the mean particle radius, with smaller particles leading to larger surface areas. For the investigated structures, tortuosity is most strongly influenced by the volume fraction of the respective phase, underlining the importance of phase connectivity for transport. These trends clarify which generator parameters predominantly control the individual target metrics and thereby support the use of the framework in a forward-design setting. As a result, the structure generation workflow can be efficiently adapted without requiring labor-intensive changes to experimental or manufacturing procedures, offering a simulation-driven path to tailoring SOFC microstructures.

3.2. Dense electrolyte layer

The multilayered SOFC microstructure includes dense layers in addition to porous ones (cf figure 4(c)). Unlike porous regions, these dense layers consist predominantly of a single material, making standard metrics such as tortuosity and SSA less informative due to their near-zero values or minimal variance. In this section, we focus on the GDC electrolyte layer as an example for such a dense layer, extracted from the experimental reconstruction (cf figure 3(a)). To enable a meaningful comparison between virtual

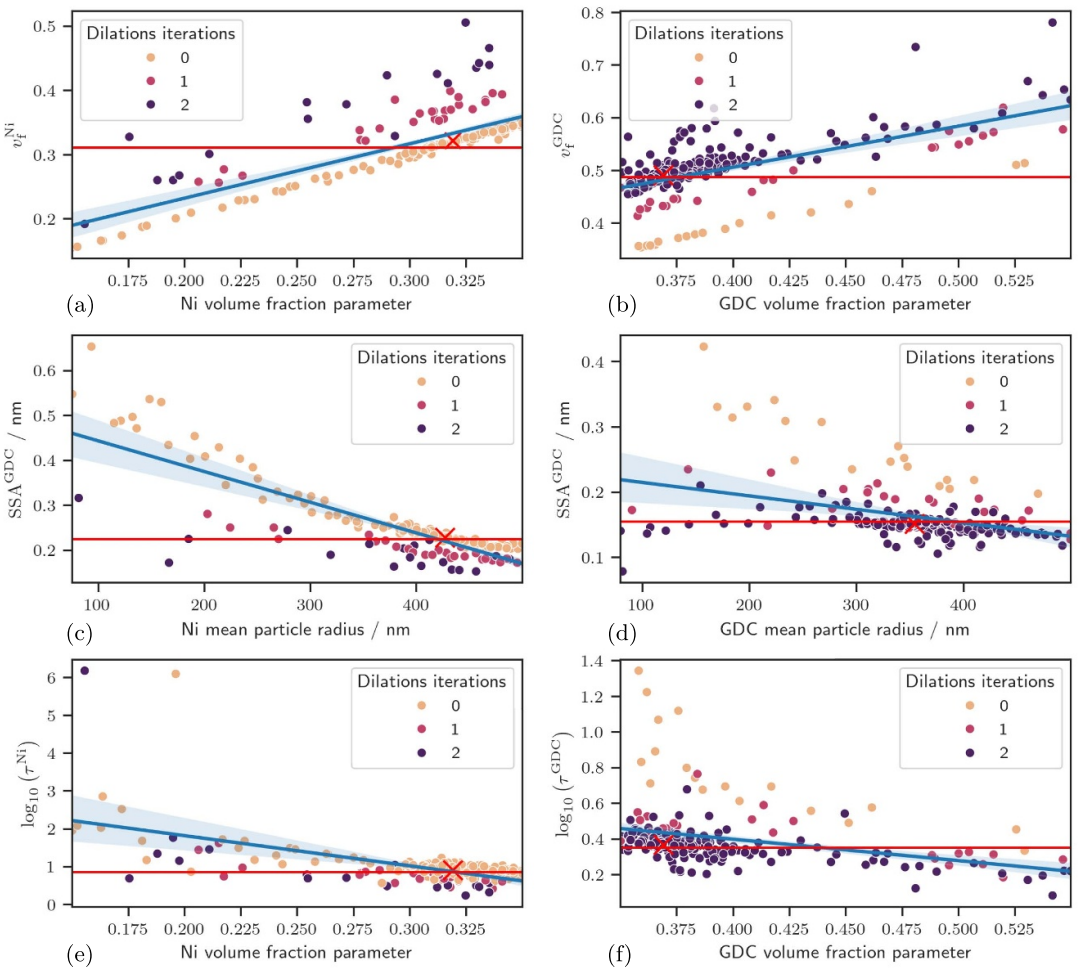

Figure 5. Correlations of input parameters versus resulting morphological metrics for the porous fuel electrode layer. Additionally, the number of dilation iterations for the corresponding material is shown in color, and the best trial is marked with a red cross. The target value is indicated with a red line. A linear regression with the confidence interval is also provided.

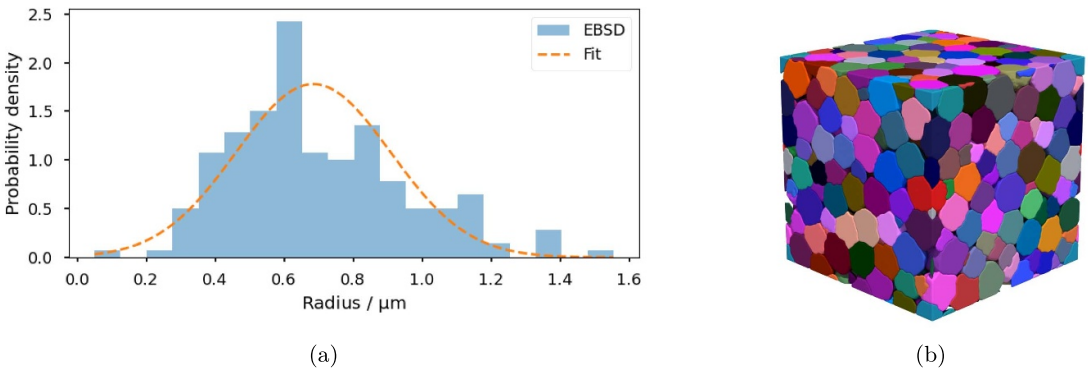

Figure 6. (a) A histogram of the equivalent radii from the EBSD measurement (see figure 3(b)) and the fitted Gaussian normal distribution for the dense GDC electrolyte layer. (b) Artificial generation of a dense GDC electrolyte layer.

and real dense microstructures, we employed an alternative metric: the equivalent radius distribution derived from 2D cross-sectional slices of the volume. This distribution, along with volume fraction and tortuosity, was used as a target for optimization. The desired radius distribution is shown in figure 6(a).

A total of 200 optimization trials were conducted to match the target metrics. The resulting artificial volume element is presented in figure 6(b) and exhibits strong visual similarity to the experimental EBSD measurement. The corresponding optimized input parameters are listed in table 2, while table 3

Table 2. Parameters for the generation of the best trial for a dense GDC electrolyte layer, cf figure 6(b).

Parameter	Unit	Value GDC
Volume fraction	%	79.19
Mean particle radius	nm	801.46
Deviation of particle radius	nm	65.86
Amplitude of angular power spectrum	W nm^{-1}	$10^{-2.5}$
Dilation iterations	—	4

Table 3. Overview of the chosen morphological metrics of the reconstructed structure for each layer, along with the artificially generated volume elements and the determined errors from comparison.

Layer	Measure	Unit	Reconstruction	Generated	Error in %
Fuel electrode	v_f^{Ni}	%	31.12	32.17	1.06
	v_f^{GDC}	%	48.79	49.14	0.35
	τ^{Ni}	—	7.30	8.05	4.89
	τ^{GDC}	—	2.26	2.34	4.05
	SSA^{Ni}	nm^{-1}	0.236	0.228	1.19
	SSA^{GDC}	nm^{-1}	0.155	0.152	2.30
Electrolyte	v_f^{GDC}	%	92.26	95.18	2.92
	τ^{GDC}	—	1.062	1.061	0.31
	σ^{GDC}	nm	224.13	230.58	2.88
	μ^{GDC}	nm	684.80	656.77	4.09
YSZ barrier	v_f^{YSZ}	%	99.55	97.63	1.92
	σ^{YSZ}	nm	224.13	224.90	0.35
	μ^{YSZ}	nm	684.80	678.69	0.89
GDC barrier	v_f^{GDC}	%	86.97	92.86	5.89
	τ^{GDC}	—	1.101	1.095	5.93
	σ^{GDC}	nm	224.13	232.73	3.84
	μ^{GDC}	nm	684.80	692.14	1.07

compares the targeted and achieved morphological metrics, including the errors. The volume fraction exhibits a higher margin of error (2.92%), compared to the porous layer, likely due to the trade-offs made during the multi-objective optimization process to balance different target metrics close to the density limit of a bulk layer.

Figure 7 illustrates corresponding parameter-response trends for the dense GDC electrolyte layer. The resulting volume fraction depends mainly on the prescribed GDC input fraction and the applied dilation steps, as shown in figure 7(a). The mean particle radius strongly influences the equivalent radius distribution, both in terms of its mean value (figure 7(b)) and its standard deviation (figure 7(d)). The tortuosity of the dense layer is again strongly affected by the volume fraction, indicating a pronounced sensitivity to small residual pore structures. Overall, these parameter–response trends help to identify which generator parameters are most relevant for reproducing the targeted morphology of dense SOFC layers.

3.3. Multilayer SOFC

To validate the structure generator's ability to reproduce a complete multilayered SOFC architecture, a virtual domain was created based on the reconstructed microstructure described in section 2.2. The layer thicknesses and overall domain dimensions were directly taken from the experimental reconstruction to ensure a consistent basis for comparison. The considered domains should therefore be understood as morphology-calibration volumes rather than as formally established representative elementary volumes. For the single-layer studies, reduced domains were chosen to preserve the voxel resolution of the reconstruction while keeping the optimization effort tractable. A formal REV convergence study and a full electrochemical validation are important next steps, but are beyond the scope of the present work. Accordingly, the present results demonstrate morphological agreement for the considered calibration volumes, but they should not yet be interpreted as a direct validation of predictive SOFC performance simulations.

To manage the high computational cost associated with generating the full multilayer structure at fixed resolution, a divide-and-conquer strategy was adopted. Each layer, whether porous or dense, was

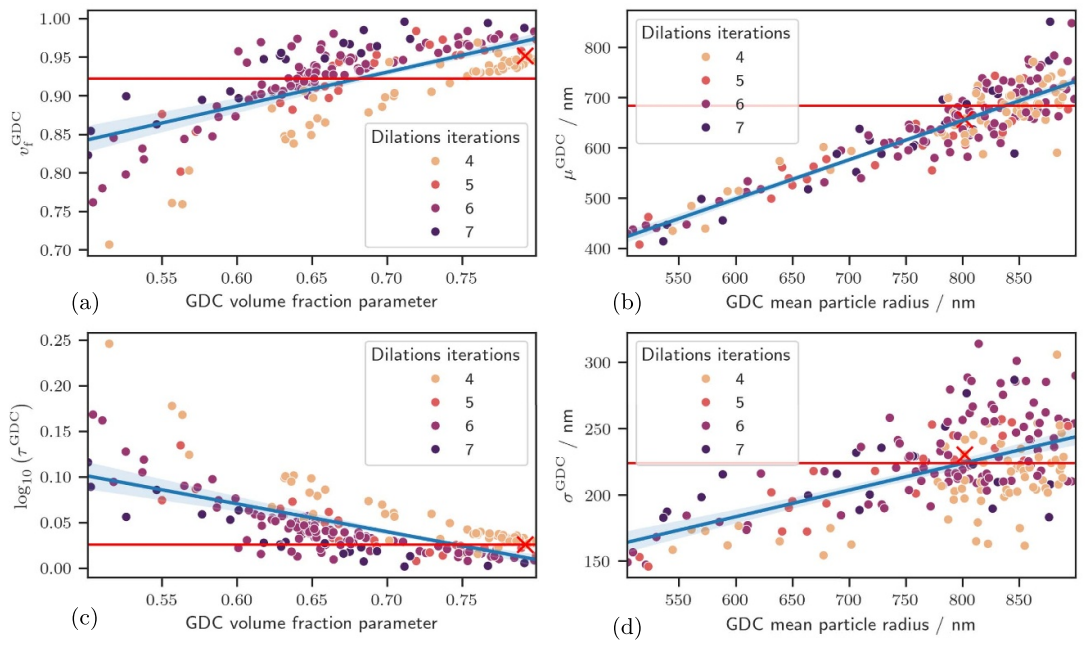

Figure 7. Correlations of input parameters versus resulting morphological metrics for the dense GDC electrolyte layer. Additionally, the number of dilation iterations for the corresponding material is shown in color, and the best trial is marked with a red cross. The target value is indicated with a red line. A linear regression with the confidence interval is also provided.

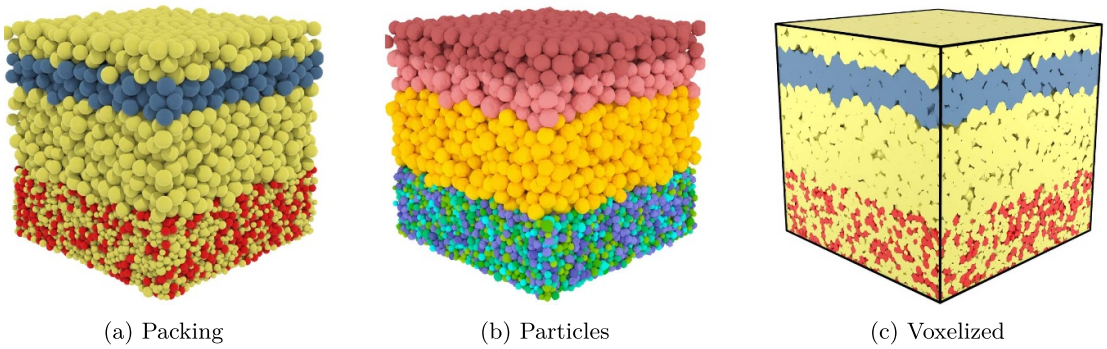

Figure 8. A generated multi-layer SOFC structure at different reconstructions stages: (a) After packing the spheres, (b) after generating the particle shapes, and (c) after the final voxelized volume element in the multiphase-field representation.

individually optimized using the previously described BO approach. For each layer, the best-performing set of input parameters was identified based on the targeted morphological metrics. The optimized parameter sets used for the multilayer generation are reported layerwise. The parameters for the fuel electrode and the dense GDC electrolyte layer are listed in tables 1 and 2, respectively, while the corresponding parameter sets for the YSZ barrier layer and the GDC barrier layer are provided in appendix (tables 4 and 5). Together, these four tables define the layer-specific input used to construct the full multilayer virtual SOFC microstructure. These optimized parameters were then combined into a single generation process, creating a full multilayer virtual SOFC microstructure with varying layer-specific characteristics. The results of this procedure are shown in figure 8, which illustrates the sequential steps of the generation process: initial particle packing, shape creation using spherical harmonics, and the final MPFM representation. When compared with the experimental reconstruction in figure 3(a), the generated microstructure exhibits strong visual and structural agreement across all layers. A detailed comparison of the morphological metrics for each layer, including volume fraction, tortuosity, SSA, and equivalent radius distribution, is provided in table 3. Among the evaluated metrics, the relative error for some tortuosity values is approximately 5%. Nevertheless, the absolute error is small, which is typical

of dense structures where even small, isolated pores impact tortuosity measurements. The observed deviation is thus acceptable, reflecting a physically reasonable sensitivity and demonstrating the accuracy and robustness of the approach for both porous and dense regions. This result confirms that the proposed structure generator can produce realistic, multilayered SOFC structures that match desired morphological characteristics. Importantly, the ability to control these features provides a basis for future systematic investigations of SOFC behavior using morphology-resolved simulation studies. For example, virtual structures with tailored morphology can be used in subsequent simulations to study stress distribution, or the coarsening behavior of nickel during operation, providing valuable insights that are otherwise difficult to obtain experimentally.

4. Conclusion

This work builds upon prior stochastic microstructure generation methods based on particle packing and spherical harmonics, particularly the frameworks of Feinauer *et al* [14] and Westhoff *et al* [60], extending them from lithium-ion battery electrodes to the more complex, multilayered architecture of SOFCs. By incorporating a discrete element method for realistic sphere packing, an enhanced neighbor graph construction for inter-particle connectivity, and a spherical harmonics-based shape generation constrained by contact points, a physics-informed and flexible virtual structure generator tailored for SOFC layers was developed. The generator was integrated with a MPFM representation and coupled to a multi-objective BO framework, enabling systematic calibration against experimentally reconstructed microstructures from FIB-SEM tomography. Morphological metrics such as volume fraction, tortuosity, SSA, and equivalent radius distributions were used as quantitative targets, allowing the approach to reproduce both porous and dense SOFC layers with high fidelity. The method was validated for individual layers as well as a complete multilayer SOFC, showing consistently low errors of $< 6\%$ across all targeted metrics and strong visual agreement with experimental reconstructions. Overall, the proposed workflow reproduces the selected target descriptors of porous and dense SOFC layers with good agreement for the considered calibration volumes, while providing a transparent framework for morphology-controlled virtual microstructure generation and calibrated multiphase-field representations for subsequent simulation studies. The developed workflow enables the efficient and systematic creation of virtual SOFC microstructures with controllable morphological characteristics, tailored for different layers within a multilayer configuration, and produces simulation-ready representations suitable for subsequent electrochemical or mechanical modeling. Future developments could incorporate additional physical processes, such as sintering kinetics, grain growth, or phase coarsening, as well as degradation-related surface effects in electrochemical materials [19], to capture microstructural evolution over time. The coupling of the generated structures with validated multiphysics simulations in fuel-cell and electrolysis modes is the subject of future work and could enable more predictive studies of structure-property relationships, thereby providing a basis for the design of optimized cell architectures.

Data availability statement

The datasets generated and analyzed during the current study were produced using the proprietary PACE3D simulation framework developed at the Karlsruhe University of Applied Sciences [25, 26], the open-source LAMMPS molecular dynamics package [56], and the open-source OPTUNA optimization framework [1]. A selected representative dataset of this work has been deposited on ZENODO [11] and is publicly accessible [51]. Due to licensing restrictions, the PACE3D source code cannot be made publicly available. However, licenses can be obtained upon request. The complete datasets, including all generated SOFC microstructures and detailed analysis results, are available upon request.

The data that support the findings of this study are openly available at the following URL/DOI: https://doi.org/10.5281/zenodo.17414137 [51].

Funding

Lukas Schöller and Luzie Wehner gratefully acknowledge the funding by the German Federal Ministry for Research, Technology and Space (BMFTR) for the ElChFest project (Elektro-chemo-mechanische Modellierung von Ceroxid-basierten Festoxidelektrolysezellen, grant number 03SF0641C). Daniel

Schneider and Britta Nestler acknowledge financial support of the Helmholtz association trough program 'MSE', No. 43.31.01.

Appendix. Optimized parameters for the GDC & YSZ barrier layer

Table 4. Parameters for the generation of the best trial for a dense YSZ barrier layer.

Parameter	Unit	Value YSZ
Volume fraction	%	78.01
Mean particle radius	nm	838.25
Deviation of particle radius	nm	89.08
Amplitude of angular power spectrum	W nm^{-1}	$10^{-2.5}$
Dilation iterations	—	6

Table 5. Parameters for the generation of the best trial for a dense GDC barrier layer.

Parameter	Unit	Value GDC
Volume fraction	%	65.38
Mean particle radius	nm	809.14
Deviation of particle radius	nm	81.97
Amplitude of angular power spectrum	W nm^{-1}	$10^{-2.5}$
Dilation iterations	—	6

ORCID iDs

Lukas Schöller 0000-0002-6616-2227
Luzie Wehner 0009-0008-5924-9157
Daniel Schneider 0000-0002-9250-2918
Ruth Schwaiger 0000-0001-8940-2361
Britta Nestler 0000-0002-3768-3277

References

[1] Akiba T, Sano S, Yanase T, Ohta T and Koyama M 2019 Optuna: a next-generation hyperparameter optimization framework *Proc. 25th ACM SIGKDD Int. Conf. on Knowledge Discovery and Data Mining*
[2] Berg T, McDonald R and Trainor R 1969 The packing of spheres *Powder Technol.* **3** 183–8
[3] Bergstra J, Bardenet R, Bengio Y and Kégl B 2011 Algorithms for hyper-parameter optimization *Advances in Neural Information Processing Systems* vol 24, ed J Shawe-Taylor, R Zemel, P Bartlett, F Pereira and K Weinberger (Curran Associates, Inc)
[4] Bezrukov A, Bargieł M and Stoyan D 2002 Statistical analysis of simulated random packings of spheres *Part. Part. Syst. Charact.* **19** 111–8
[5] Bond S D and Leimkuhler B J 2008 Stabilized integration of Hamiltonian systems with hard-sphere inequality constraints *SIAM J. Sci. Comput.* **30** 134–47
[6] Burnett T, Kelley R, Winiarski B, Contreras L, Daly M, Gholinia A, Burke M and Withers P 2016 Large volume serial section tomography by Xe plasma FIB dual beam microscopy *Ultramicroscopy* **161** 119–29
[7] Connor P A *et al* 2018 Tailoring SOFC electrode microstructures for improved performance *Adv. Energy Mater.* **8** 1800120
[8] Cooper S, Bertei A, Shearing P, Kilner J and Brandon N 2016 Taufactor: an open-source application for calculating tortuosity factors from tomographic data *SoftwareX* **5** 203–10
[9] Cundall P A and Strack O D L 1979 A discrete numerical model for granular assemblies *Géotechnique* **29** 47–65
[10] Ender M, Joos J, Carraro T and Ivers-Tiffée E 2012 Quantitative characterization of LiFePO 4 cathodes reconstructed by FIB/SEM tomography *J. Electrochem. Soc.* **159** A972–80
[11] European Organization For Nuclear Research and OpenAIRE 2013 Zenodo
[12] Fager C, Röding M, Olsson A, Lorén N, von Corswant C, Särkkä A and Olsson E 2020 Optimization of FIB-SEM tomography and reconstruction for soft, porous and poorly conducting materials *Microsc. Microanal.* **26** 837–45
[13] Fan L, Reder M, Schneider D, Hinterstein M and Nestler B 2023 A phase-field model for ferroelectric materials—based on the multiphase-field method *Comput. Mater. Sci.* **230** 112510
[14] Feinauer J, Brereton T, Spettl A, Weber M, Manke I and Schmidt V 2015 Stochastic 3D modeling of the microstructure of lithium-ion battery anodes via Gaussian random fields on the sphere *Comput. Mater. Sci.* **109** 137–46

[15] Garboczi E 2002 Three-dimensional mathematical analysis of particle shape using x-ray tomography and spherical harmonics: application to aggregates used in concrete *Cem. Concr. Res.* **32** 1621–38
[16] Gayon-Lombardo A, Mosser L, Brandon N P and Cooper S J 2020 Pores for thought: generative adversarial networks for stochastic reconstruction of 3D multi-phase electrode microstructures with periodic boundaries *npj Comput. Mater.* **6** 82
[17] Gilbert E N 1964 Randomly packed and solidly packed spheres *Can. J. Math.* **16** 286–98
[18] Gonzalez R C and Woods R E 2018 *Digital Image Processing* 4th edn (Pearson)
[19] Hanif M B *et al* 2024 Innovative advances and challenges in solid oxide electrolysis cells: exploring surface segregation dynamics in perovskite electrodes *Mater. Sci. Eng. R Rep.* **161** 100864
[20] Hill R 1952 The elastic behaviour of a crystalline aggregate *Proc. Phys. Soc. A* **65** 349–54
[21] Hobson E W 1955 *The Theory of Spherical and Ellipsoidal Harmonics* (Cambridge University Press)
[22] Hoffrogge P W, Schneider D, Wankmüller F, Meffert M, Gerthsen D, Weber A, Nestler B and Wieler M 2023 Performance estimation by multiphase-field simulations and transmission-line modeling of nickel coarsening in FIB-SEM reconstructed Ni-YSZ SOFC anodes I: influence of wetting angle *J. Power Sources* **570** 233031
[23] Hsu T, Epting W K, Kim H, Abernathy H W, Hackett G A, Rollett A D, Salvador P A and Holm E A 2021 Microstructure generation via generative adversarial network for heterogeneous, topologically complex 3D materials *JOM* **73** 90–102
[24] Hussain S and Yangping L 2020 Review of solid oxide fuel cell materials: cathode, anode and electrolyte *Energy Transitions* **4** 113–26
[25] Hötzer J, Rehn V, Rheinheimer W, Hoffmann M J and Nestler B 2016 Phase-field study of pore-grain boundary interaction *J. Ceram. Soc. Japan* **124** 329–39
[26] Institute of Digital Materials Science (IDM) 2025 Karlsruhe university of applied sciences. Pace3D – a parallel phase-field framework (Accessed 10 October 2025)
[27] Ishfaq H A, Rehman S U, Khan M Z, Sattar T, Saleem M, Koh J-H, Hussain I, Hussain A, Qamar S and Ghaffar A 2025 Superior oxygen reduction performance and stability of SOFC cathodes via RF-sputtered ruthenium electrocatalysts *ACS Appl. Energy Mater.* **8** 15069–78
[28] Mościński Z A R J, Bargieł M and Jacobs P W M 1989 The force-biased algorithm for the irregular close packing of equal hard spheres *Mol. Simul.* **3** 201–12
[29] Jodrey W S and Tory E M 1979 Simulation of random packing of spheres *Simulation* **32** 1–12
[30] Jodrey W S and Tory E M 1985 Computer simulation of close random packing of equal spheres *Phys. Rev. A* **32** 2347–51
[31] Kannenberg T, Schöller L, Prahs A, Schneider D and Nestler B 2023 Investigation of microstructure evolution accounting for crystal plasticity in the multiphase-field method *PAMM* **23** e202300138
[32] Kim S G, Kim D I, Kim W T and Park Y B 2006 Computer simulations of two-dimensional and three-dimensional ideal grain growth *Phys. Rev. E* **74** 061605
[33] Kruskal J B 1956 On the shortest spanning subtree of a graph and the traveling salesman problem *Proc. Am. Math. Soc.* **7** 48–50
[34] Kwon B-S, Khan M Z, Joh D-W, Song R-H, Kim T-H, Lim T-H, Hong J-E and Park S-J 2026 Mechanically robust and electrochemically stable Ni-3YSZ anode supported solid oxide fuel cell achieved through Nano-SiC engineering *J. Power Sources* **661** 238574
[35] Lee J-H, Heo J-W, Lee D-S, Kim J, Kim G-H, Lee H-W, Song H and Moon J-H 2003 The impact of anode microstructure on the power generating characteristics of SOFC *Solid State Ion.* **158** 225–32
[36] Leech J 1967 Notes on sphere packings *Can. J. Math.* **19** 251–67
[37] McGEARY R K 1961 Mechanical packing of spherical particles *J. Am. Ceram. Soc.* **44** 513–22
[38] Mehdi M *et al* 2023 Progress and prospects in direct ammonia solid oxide fuel cells *Russ. Chem. Rev.* **92** RCR5030
[39] Mehran M T, Kim T-H, Khan M Z, Lee S-B, Lim T-H and Song R-H 2019 Highly durable nano-oxide dispersed ferritic stainless steel interconnects for intermediate temperature solid oxide fuel cells *J. Power Sources* **439** 227109
[40] Nestler B, Garcke H and Stinner B 2005 Multicomponent alloy solidification: Phase-field modeling and simulations *Phys. Rev. E* **71** 041609
[41] Niu Z, Zhao W, Wu B, Wang H, Lin W-F, Pinfield V J and Xuan J 2023 π learning: a performance-informed framework for microstructural electrode design *Adv. Energy Mater.* **13** 2300244
[42] Niu Z, Zhou Z, Perrenot P, Villevieille C, Zhao W, Cai Q, Pinfield V J and Wang Y 2025 Seeing the middle: reconstructing 3D internal electrode microstructures from low-resolution surfaces with generative diffusion artificial intelligence *Small Sci.* **5** 2500414
[43] Ozaki Y, Tanigaki Y, Watanabe S, Nomura M and Onishi M 2022 Multiobjective tree-structured parzen estimator *J. Artif. Intell. Res.* **73** 1209–50
[44] Ozaki Y, Tanigaki Y, Watanabe S and Onishi M 2020 Multiobjective tree-structured parzen estimator for computationally expensive optimization problems *Proc. 2020 Genetic and Evolutionary Computation Conf., GECCO '20* (Association for Computing Machinery) pp 533–41
[45] Prahs A, Schneider D and Nestler B 2025 A continuum thermodynamic approach to the phase-field method: the order parameter as internal state variable *Contin. Mech. Thermodyn.* **37** 55
[46] Ramler D 2026 Development of an oxygen ion conducting solid oxide electrolysis cell based on gadolinium-doped cerium oxide as fuel electrode and electrolyte material *Dissertation* RWTH Aachen University
[47] Reder M, Prahs A, Schneider D and Nestler B 2024 Viscous stress approximations in diffuse interface methods for two-phase flow based on mechanical jump conditions *Comput. Methods Appl. Mech. Eng.* **432** 117341
[48] Rehman J, Hanif M B, Khan M Z, Ullah M, Starostina I A, Muhammad M T and Li Z 2024 A review of proton-conducting electrolytes for efficient low-temperature solid oxide fuel cells: progress, challenges and perspectives *Energy Fuels* **38** 22637–65
[49] Schoof E, Schneider D, Streichhan N, Mittnacht T, Selzer M and Nestler B 2018 Multiphase-field modeling of martensitic phase transformation in a dual-phase microstructure *Int. J. Solids Struct.* **134** 181–94
[50] Schöller L, Schneider D, Herrmann C, Prahs A and Nestler B 2022 Phase-field modeling of crack propagation in heterogeneous materials with multiple crack order parameters *Comput. Methods Appl. Mech. Eng.* **395** 114965
[51] Schöller L, Wehner L, Schneider D, Schwaiger R and Nestler B Virtual design of multilayered SOFC microstructures based on particle packing and spherical harmonics – representative dataset, 2025.
[52] Silbert L E, Ertaş D, Grest G S, Halsey T C, Levine D and Plimpton S J 2001 Granular flow down an inclined plane: Bagnold scaling and rheology *Phys. Rev. E* **64** 051302
[53] Song C, Wang P and Makse H A 2008 A phase diagram for jammed matter *Nature* **453** 629–32

[54] Steinbach I and Pezzolla F 1999 A generalized field method for multiphase transformations using interface fields *Physica D* **134** 385–93
[55] Sun Y and Beckermann C 2007 Sharp interface tracking using the phase-field equation *J. Comput. Phys.* **220** 626–53
[56] Thompson A P *et al* 2022 LAMMPS - a flexible simulation tool for particle-based materials modeling at the atomic, meso and continuum scales *Comp. Phys. Commun.* **271** 108171
[57] Torquato S and Stillinger F H 2010 Jammed hard-particle packings: from Kepler to Bernal and beyond *Rev. Mod. Phys.* **82** 2633–72
[58] Verlet L 1967 Computer "experiments" on classical fluids. I. thermodynamical properties of lennard-jones molecules *Phys. Rev.* **159** 98–103
[59] Wankmüller F 2021 Mehrskalige charakterisierung der hochtemperatur-brennstoffzelle (SOFC) *PhD* Karlsruher Institut für Technologie (KIT), Karlsruhe
[60] Westhoff D, Manke I and Schmidt V 2018 Generation of virtual lithium-ion battery electrode microstructures based on spatial stochastic modeling *Comput. Mater. Sci.* **151** 53–64
[61] Wieczorek M A and Meschede M 2018 SHTools: tools for working with spherical harmonics *Geochem. Geophys. Geosyst.* **19** 2574–92
[62] Xu C S, Hayworth K J, Lu Z, Grob P, Hassan A M, García-Cerdán J G, Niyogi K K, Nogales E, Weinberg R J and Hess H F 2017 Enhanced FIB-SEM systems for large-volume 3D imaging *eLife* **6** e25916
[63] Yan Z, He A, Hara S and Shikazono N 2019 Modeling of solid oxide fuel cell (SOFC) electrodes from fabrication to operation: microstructure optimization via artificial neural networks and multi-objective genetic algorithms *Energy Convers. Manage.* **198** 111916
[64] Yeong C L Y and Torquato S 1998 Reconstructing random media *Phys. Rev. E* **57** 495–506
[65] Yeong C L Y and Torquato S 1998 Reconstructing random media. II. three-dimensional media from two-dimensional cuts *Phys. Rev. E* **58** 224–33
[66] Golkhatmi S Z, Asghar M I and Lund P D 2022 A review on solid oxide fuel cell durability: latest progress, mechanisms and study tools *Renew. Sustain. Energy Rev.* **161** 112339
[67] Zhu H, Zhou Z, Yang R and Yu A 2007 Discrete particle simulation of particulate systems: theoretical developments *Chem. Eng. Sci.* **62** 3378–96
[68] Zhu H, Zhou Z, Yang R and Yu A 2008 Discrete particle simulation of particulate systems: a review of major applications and findings *Chem. Eng. Sci.* **63** 5728–70